JOURNAL OF MATERIALS SCIENCE 24 (1989) 590–598

Gas atomization of cobalt ferrite–phosphate melts

MARK R. DE GUIRE*, R. C. O'HANDLEY, G. KALONJI
Department of Materials Science and Engineering, Massachusetts Institute of Technology, Cambridge, Massachusetts 02139, USA

A rapidly solidified $(Co, Fe)_3O_4$ spinel was formed in a cobalt–iron–phosphate glass matrix by gas atomization of melts of composition 37.5% mol% CoO, 37.5% Fe_2O_3, 25% P_2O_5; and 40% CoO, 40% Fe_2O_3, 20% P_2O_5, and the material has been characterized using size analysis, X-ray diffraction, Mössbauer spectroscopy, and scanning electron microscopy with energy dispersive X-ray spectroscopy.

In the 20 mol% P_2O_5 composition, atomized powder 50–100 μm in diameter contained 33 wt% $(Co, Fe)_3O_4$. The ferrite crystallized as randomly oriented, faceted dendrites parallel to $\langle 1\,0\,0 \rangle$, and the growth was apparently diffusion controlled. Unlike the ferrite, where iron is in both tetrahedral and octahedral coordination, the iron in the glassy matrix was predominantly in distorted octahedral coordination. Overall particle size distributions were broad (15–700 μm), with $\sim$50 wt% smaller than 200 μm. The maximum in the size distribution shifted from 150 to 80 μm on increasing the atomizing pressure from 7 to 20 bar (100 to 300 psi). Calculations have shown that the cooling rates obtained with oxide melts vary strongly with droplet size, and less strongly with melt temperature.

1. Introduction

Rapid solidification techniques allow cooling rates of 10^3–10^8 °C sec^{-1} to be applied to molten materials, compared to a maximum of 10^3 °C sec^{-1} encountered in various conventional melt solidification processes. These high cooling rates have many important advantages in materials processing; here we focus on the ability to produce metastable crystalline and glassy phases, using gas atomization on melts in the system $CoFe_2O_4$–P_2O_5.

While rapid solidification has been an active area of research in metallurgy for over twenty years, much less attention has been directed toward the rapid solidification of oxides. Nevertheless, in the last $\sim$15 years, virtually every rapid solidification technique has been attempted with non-metals, as indicated in the review by Revcolevschi and Livage [1].

This work was part of a program whose goal was to obtain fine spinel ferrite particles with unique morphologies and properties, with potential application as a recording medium or (when embedded in an oxide glass matrix) as a powder precursor for magnetic glass ceramics. This paper describes the physical and structural characterization of atomized $CoFe_2O_4$–P_2O_5 materials, and is, to our knowledge, the first detailed description of atomization of oxides in the literature. Cooling rates were calculated as a function of droplet size, and atomizing pressure was varied to study its effect on particle size. Then the particles' microstructures and iron coordination states were studied as a function of particle size using electron microscopy and Mössbauer spectroscopy, to see if the calculated cooling rates correlated with the observed ferrite content and morphology. The effect of rapid solidification on the cation distribution and magnetic properties of the precipitated $(Co, Fe)_3O_4$ spinel will be reported elsewhere [2].

1.1. Overview of gas atomization

Gas atomization is a rapid solidification technique in which high-pressure gas hits a falling melt stream. Atomization achieves high cooling rates (dT/dt) by (1) overcoming the surface tension of the liquid to form tiny droplets, through which heat will flow quickly to the surface, and (2) increasing the relative velocity between gas and droplet, raising the rate of heat transfer through the gas–droplet boundary layer.

Ideally, the droplets solidify before colliding with each other or the chamber walls. Thus, unlike many rapid solidification techniques, atomization does not require contact of the melt with a solid surface. While the cooling rates for conventional atomization are usually lower than for other methods [3, 4], the decreased likelihood of heterogeneous nucleation can result in a higher degree of undercooling. This can cause a higher solidification front velocity, solute trapping, and in general a larger departure from equilibrium. Atomization also produces, in one processing step, fine powders of controllable size distributions, with compositions and microstructures often unobtainable by other powder production techniques.

* *Present address*: Department of Materials Science and Engineering, Case Western Reserve University, Cleveland, Ohio, 44106, USA.

0022–2461/89 $03.00 + .12

Analyses of the fluid dynamics of atomization have focused primarily on the droplet diameter and size distribution. In general, average particle size decreases with decreasing melt stream diameter, melt flow rate, melt kinematic viscosity, and melt surface tension, and with increasing melt density, gas velocity, gas flow rate, and gas kinematic viscosity. These dependences have been quantified in empirical relations [5]. Generally, average powder size decreases with increasing atomization pressure [6] through its effect on increasing gas flow rate. In commercial atomization, melt flow rates of 10–60 g sec^{-1}, gauge pressures of 50–80 bar (800–1200 psi) and gas flow rates of 2.5–3.8 $\times$ 10^4 cm^3 sec^{-1} (50–80 cfm) are typical [7].

As the temperature of the cooling droplets depends on their size (as discussed below), the cooling rates obtainable in atomization are complex and incompletely understood functions of material properties and processing variables. Furthermore, the temperature dependence of the gas and melt thermal conductivities, and the time-dependent temperature profile across the gas and melt, would also have to be considered in a precise analysis. The simplifying assumptions made in the present cooling rate calculations are discussed in the following section.

In atomization of aluminium alloys, heat transfer is limited by convection away from the droplet surface [8]. With oxides,which have much lower thermal conductivities, heat conduction through the droplet will partially or completely limit the cooling rate. In either case, a strong dependence on particle size is expected. The higher melting points of oxides require that heat loss by radiation be taken into account when determining the cooling rate.

1.2. Cooling rate calculations

Birnie has written computer programs [9] to solve a series expression for the cooling rate experienced by materials as a function of materials properties, quench medium and conditions, sample size, and temperature. The version used here assumed black-body radiation. It calculates the cooling rates for the centre of an infinite slab of thickness $2L$, which here will be assumed to be equivalent to the diameter, D, of an atomized particle. (Since a slab cools in one direction and a sphere in three, one would expect this assumption to underestimate the actual cooling rate.) The other input consists of values of starting sample temperature, temperature of the quench medium, heat transfer coefficient, h, for the quench medium, and sample properties thermal conductivity, k, density ϱ, and heat capacity, C_p.

To estimate the cooling rates during atomization of $CoFe_2O_4$–P_2O_5 melts, and to determine the comparative effects of droplet size and temperature, values of C_p (0.3 cal g^{-1} °C^{-1}), and k (0.005 cal cm^{-1} sec^{-1} °C^{-1}) typical for silicate glasses [9] were used. Melt density ϱ was estimated to be 3.8 g cm^{-3}. These properties were assumed to be independent of temperature, composition, and extent of crystallization. The atomizing gas was assumed to stay at 20° C during atomization, and hence the temperature dependence of the gas properties was ignored. The uncertainty [9] in the calculations is estimated to be $\pm$25%.

The heat transfer coefficient h depends on properties of the gas, the particle diameter, and gas velocity, To represent the conditions during atomizing, it is desirable to calculate h as a function of particle diameter D, using

$$h = k_g N_{Nu}/D \quad (1)$$

where k_g is the thermal conductivity of the gas, 3.5 $\times$ 10^{-4} cal cm^{-1} sec^{-1} °C^{-1} for helium [10], N_{Nu} is the Nusselt number (dimensionless), computed using the Ranz-Marshall correlation [11] for a fluid flowing past a sphere:

$$N_{Nu} = 2.0 + 0.6 N_{Re}^{1/2} N_{Pr}^{1/3} \quad (2)$$

where N_{Pr} is the Prandtl number, 0.68 for helium [12]. Process variables affect h through N_{Re}, the Reynolds number:

$$N_{Re} = Dv\varrho_g/\mu_g \quad (3)$$

where v is the relative velocity between the gas and the droplet; μ_g is the gas absolute viscosity, 1.9 $\times$ 10^{-4} g cm^{-1} sec^{-1} for helium [10, 12], and ϱ_g is the gas density, 1.6 $\times$ 10^{-4} g cm^{-3} for helium [12].

In the current work, v is the only parameter in Equations 1–3 that was not explicitly known. A constant velocity of 1000 cm sec^{-1} was assumed. The likely dependence of v on D was ignored. Increasing v by an order of magnitude increased h by at most a factor of 2.5 for $D < 100\,\mu$m.

When gas flows past a sphere, the heat transfer coefficient h varies along the surface, being highest at the point of gas impingement and decreasing by as much as an order of magnitude on the opposite surface [11]. A correction for this effect was not attempted in this work, since the atomizing gas would be expected to spin most of the droplets, resulting in an approximately uniform h over the spherical surface.

2. Experimental procedure

Spinel ferrites have melting points above 1600° C, prohibitively high for the available experimental apparatus. P_2O_5 was chosen as a flux for $CoFe_2O_4$ because: (1) it would form reasonably fluid, lower temperature melts; (2) it could form a glassy matrix after solidification; (3) it would not alloy with the spinel structure. The two $CoFe_2O_4$–P_2O_5 compositions chosen were 37.5 mol % CoO, 37.5% Fe_2O_3, 25% P_2O_5 (CFP25), with liquidus temperature 1385° C; and 40% CoO, 40% Fe_2O_3, 20% P_2O_5 (CFP20), with liquidus temperature 1435° C [13].

10–15 g of sintered powder were placed in a platinum crucible, 35 mm diameter by 35 mm tall. A dense alumina disc was cemented to the top of the crucible. A four-hole alumina thermocouple tube was cemented to a hole in the centre of this disc. A Pt/Pt–13% Rh thermocouple was threaded through two holes in the tube, and argon ejection gas could be sent through the other holes by switching on a solenoid valve. Crucible, lid, and inlet tube were surrounded by alumina fibreboard insulation to form a cylinder 5 cm in diameter by 9 cm tall, with the bottom of the crucible 13 mm

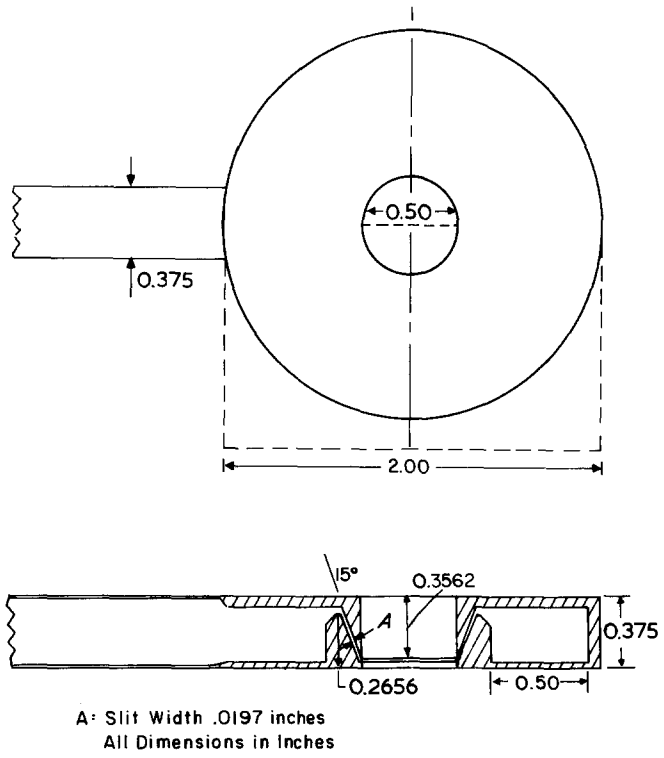

Figure 1 Conical atomizing nozzle used in the current work. *A* is the slit width = 0.0197 inches. All dimensions in inches (1 inch = 2.54 cm).

from the bottom of the insulation. This crucible holder sat directly on the atomization nozzle during melting and atomization.

Fig. 1 shows the atomizing nozzle used in this work. Gas leaves the nozzle through a 0.5 mm conical slit, to insure a common point of impingement on the melt stream. The comparatively large slit area permits a higher gas flow rate than does the more common discrete hole design. Therefore, to prevent the atomizing gas from blowing the melt stream back up towards the crucible, a steep inclination of the gas jet of 15° from vertical is required, compared to a typical angle of 30° for discrete holes of 0.5 mm diameter.

Fig. 2 shows the atomizing chamber. The position of the atomization nozzle is indicated through the front viewport. The nozzle is shown without the crucible on it, to show the circular feed-through for the heating source. The powder was melted using induction heating, with the platinum crucible serving as the susceptor. About 1.5 kW was sufficient to achieve a heating rate of $\sim 40°\,C\,sec^{-1}$ from 200 to $\sim 1300°\,C$. When the melt reached 20–120° C above its liquidus temperature, 0.3 bar (5 psi) of argon was introduced into the crucible to force the melt through a 0.635 mm hole in the crucible bottom. As soon as melt emerged from the crucible, the helium atomization gas at 7–20 bar (100–300 psi) (measured during atomization by a high-precision pressure gauge) was released by switching on another solenoid valve. Atomization was usually complete in less than about 10 sec. The powder-laden gas entered a cyclone powder collector, where the powder settled into a cup and the gas was exhausted through a submicron filter.

Powder diameters were determined by sieving, using standard sieve sizes from 53–710 μm. The only material examined in detail was powder from the collector cup, which represented yields of 8 to 40% of the starting powder. Appreciable amounts of material could be collected from ledges and crevices in the chamber, but this powder was of irregular shape and surface quality, and was found to contain more crystalline material and different crystalline phases than cycloned powder of similar size.

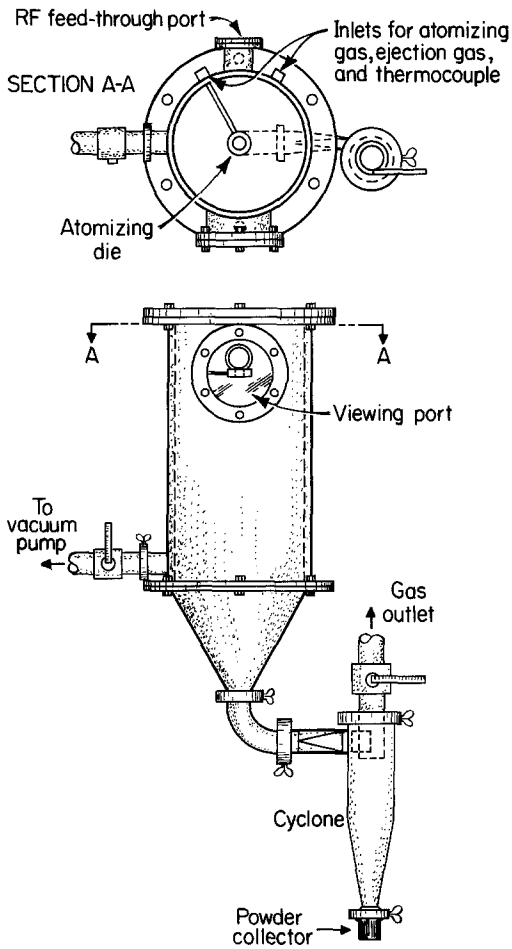

Figure 2 Laboratory-scale atomizing chamber used in the present work. Inner diameter = 30.5 cm.

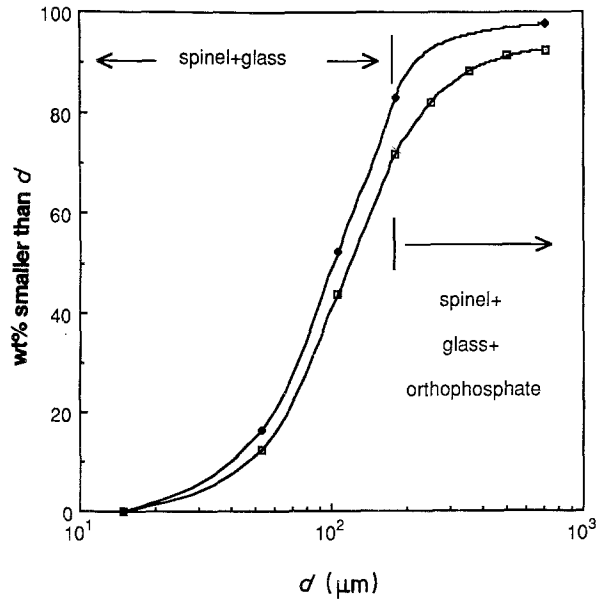

Figure 3 Cumulative particle size distribution in rapidly solidified 40 mol % CoO–40% Fe_2O_3–20% P_2O_5 (◆ CFP20) and 37.5% CoO–37.5% Fe_2O_3–25% P_2O_5 (□ CFP25). Atomizing pressure was 100 psi for CFP25 and 300 psi for CFP20.

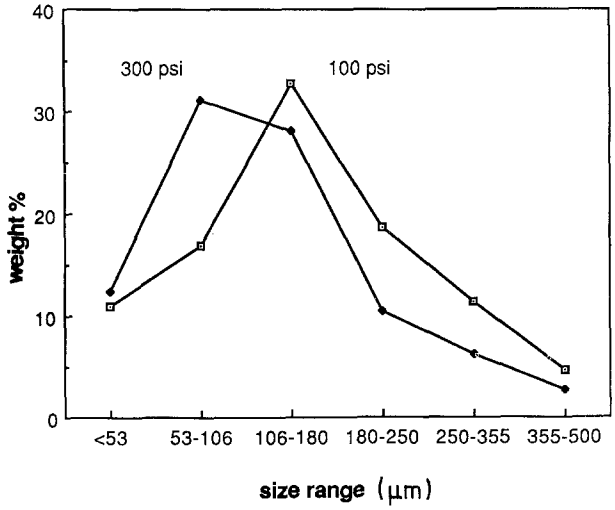

Figure 4 Particle size distribution by range, as a function of atomizing pressure, in rapidly solidified 37.5% CoO–37.5% Fe_2O_3–25% P_2O_5 (CFP25). (◆ 300 psi, □ 100 psi).

Debye–Scherrer X-ray diffraction with Co Kα, radiation and iron filter was performed on atomized powder samples of various sizes.

Room temperature Mössbauer spectroscopy was used to determine the valence and coordination state of iron in the Co–Fe–phosphate glass matrix, and to determine the proportions of crystalline and glassy material as a function of powder size in the atomized powder.

In Mössbauer spectroscopy, the signal-to-noise ratio and counting rate are optimized [14] at an iron concentration of $\sim 7\,mg\,cm^{-2}$. If, as in the present work, the materials studied are relatively rich in iron, they can be mixed with an iron-free substance to achieve the desired iron concentration. To this end, the atomized powders of various size ranges were mixed with sugar and ground under acetone in a mortar and pestle.

Mössbauer data were taken at room temperature. Our technique has been described elsewhere [13]. The fits were constrained so that the two peaks of a doublet had equal areas and widths and the area ratio of the peaks in a sextet was 3:2:1:1:2:3. Isomer shifts were measured relative to the midpoint and gradient of an iron foil spectrum.

3. Results and discussion

3.1. Particle size

Fig. 3 shows cumulative particle size distributions obtained for CFP25 and CFP20. About 50 wt % of the material was smaller than 100 μm and none was smaller than 15 μm. Debye–Scherrer X-ray diffraction showed that material smaller than 180 μm consisted of $(Co, Fe)_3O_4$ in a cobalt–iron–phosphate glass. Larger particles showed weak X-ray lines from another crystalline phase, tentatively identified as a cobalt-divalent iron orthophosphate.

X-ray diffraction of material smaller than 30 μm showed that none of the atomized material was completely glassy. This might be expected from results of Sugimoto and coworkers [15], who reported a glass-forming limit of 36 mol % Fe_2O_3, 36% CoO, 28% P_2O_5 using steel twin rollers, a technique which usually gives higher cooling rates for oxides than atomization. Percent crystallinity is discussed in more detail in the analysis of the Mössbauer spectra.

Fig. 4 shows that for the present nozzle design and a fixed melt composition (CFP25), particle size

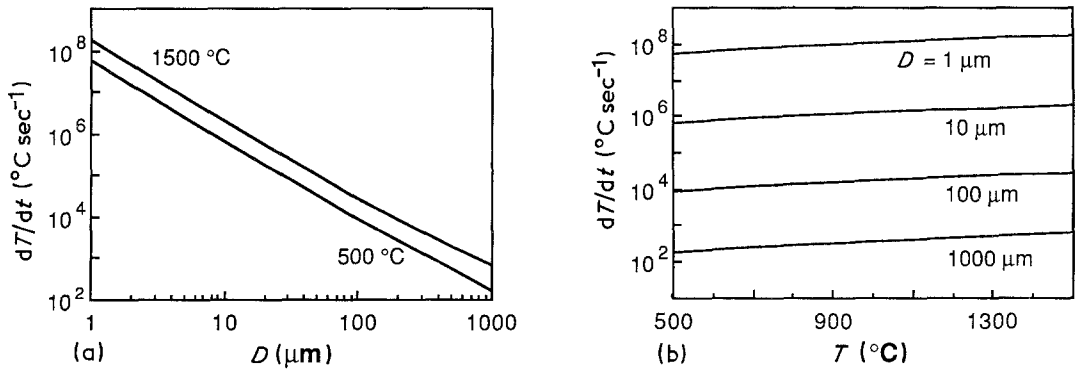

Figure 5 Cooling rates calculated for gas atomization of oxide melts in helium, assuming density of $3.8\,g\,cm^{-3}$, thermal conductivity of $0.005\,cal\,cm^{-1}\,°C^{-1}$, heat capacity of $0.3\,cal\,g^{-1}\,°C^{-1}$), and gas velocity of 1000 cm sec^{-1}. (a) Dependence of cooling rate on droplet diameter. (b) Temperature dependence of cooling rate.

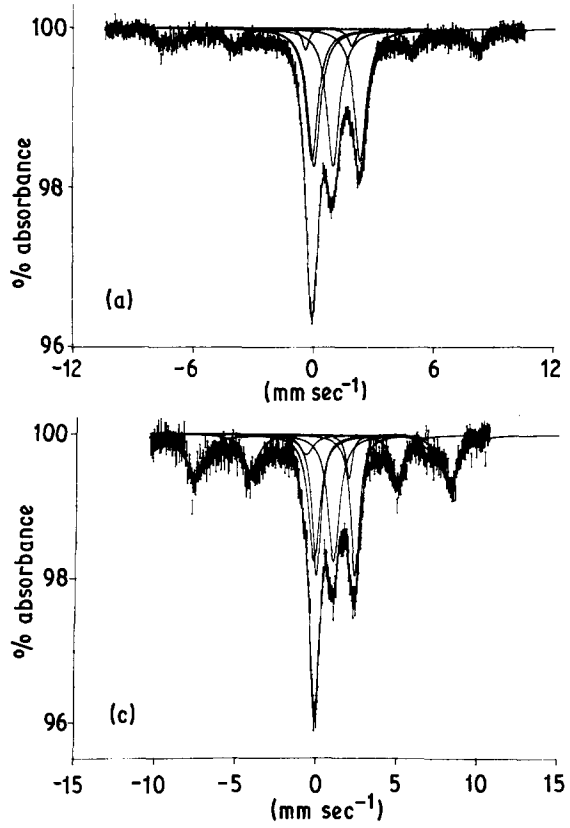

distribution shifted to smaller sizes with increasing atomizing pressure. This is as expected, because calculations show [7] that droplet diameters scale with the ratio of melt flow rate to gas flow rate.

3.2. Cooling rates during atomization of oxides

Using the relations for heat transfer coefficient presented in the introduction, and Birnie's [9] computer programs, cooling rates were calculated as a function of particle size and melt temperature (Fig. 5). In light of the assumptions (discussed in the introduction) inherent in the use of these programs, the results are more useful for illustrating trends than for providing accurate cooling rates. Still, the rates obtained agree reasonably well with measured values and with other calculations [3, 4].

Heat loss from radiation, which was included in the calculations, is proportional to T^4, and droplets have a high ratio of radiating surface to volume. However, the calculated dependence of the cooling rate on droplet temperature was relatively weak (Fig. 5). This indicates that radiation was not a significant source of the heat transfer under the assumed conditions, but recall that these included slab rather than spherical geometry. However, whereas the slab model may have underestimated the temperature dependence of cooling rate, the assumption of temperature-invariant droplet thermal conductivity may have overestimated it. As the solid is formed, the effective droplet thermal conductivity should increase, counteracting the effect of decreasing temperature difference between gas and droplet during atomization.

The dominant parameter affecting cooling rate in oxide melts is seen to be particle size, with a size change of three orders of magnitude causing a change of five orders in cooling rate.

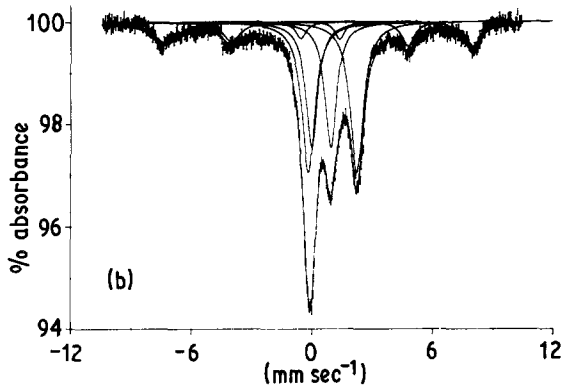

Figure 6 Room temperature Mössbauer spectra of atomized CFP25 of different particle sizes. (a) < 53 μm, (b) 53–106 μm, (c) 106–180 μm.

3.3. Mössbauer spectroscopy

3.3.1. Extent of crystallization

All the atomized powder smaller than 180 μm was known to consist only of cobalt–iron–phosphate glass and ferrite. The central regions of the Mössbauer spectra (Figs 6 and 7) were fit with two doublets, one each for Fe^{2+} and Fe^{3+} in the glass. (Two absorptions, one from each doublet, overlap to form the large middle peak.) The outer regions of the spectra arise from iron in the spinel. This phase contains several distinct iron environments, each with a characteristic six-peak pattern. These overlapping sextets could only be fit to a single six-peak envelope (except in one spectrum, discussed below). Although the curve fit provided a reliable area for this envelope in each spectrum, the isomer shifts, quadrupole splittings and linewidths are not useful for diagnosing the iron valence and coordination in the spinel. These parameters are therefore omitted from Table I.

The fractions of iron in the spinel phase in atomized CFP25 and CFP20 as a function of particle size (Fig. 8) were obtained by comparing the areas of the peaks from the glassy and crystalline phases. It was assumed that the ^{57}Fe recoilless fraction was the same in the glass and the crystal. The data of Fig. 8 are not equal to the fraction of spinel in the atomized powder; the compositions of the atomized spinels [2] were not generally $CoFe_2O_4$ and the iron content changed with particle size. However, the measured variation in spinel iron content with particle size was small compared to the variations shown in Fig. 8. Nevertheless, since only one of the spinel compositions of the powders reported here is known, the data in Fig. 8 should be regarded as a qualitative indication of the variation of spinel content with particle size.

As would be expected from the cooling rate calculations, the amount of crystalline material increased with increasing particle size. For the particle size ranges studied, CFP20 contained up to twice as much spinel as CFP25. This could be caused by the higher liquidus temperature and presumably lower viscosity of CFP20, both of which would enhance crystallization rates, and simply by the higher concentration of $CoFe_2O_4$ in CFP20 (the lever rule).

The ratios of iron in the glass and ferrite can be used to calculate the weight fraction of ferrite as a function of particle size if the ferrite composition is known. For

TABLE I Room temperature isomer shifts ($\delta \pm 0.02\,mm\,sec^{-1}$ relative to iron foil), quadrupole splittings (Δ, $\pm 0.03\,mm\,sec^{-1}$), linewidths (Γ, $\pm 0.1\,mm\,sec^{-1}$*), magnetic hyperfine field (MHF, $\pm 3\,kOe$), and % area ($\pm 2\%$) for atomized $CoFe_2O_4$-P_2O_5 powders of diameter d. All fits were constrained so that doublets have equal widths and areas, and that sextets have area ratios 3:2:1:1:2:3.

d, μm	δ	Δ	Γ	MHF	% area	Assignment
37.5 mol % CoO, 37.5% Fe_2O_3, 25.0% P_2O_5 (CFP25)						
< 53	0.44	1.05	0.76		41.7	Fe^{3+} octahedral, glass
	1.16	2.31	0.72		37.9	Fe^{2+} octahedral, glass
					20.3	Fe^{2+} and Fe^{3+}, $(Co, Fe)_3O_4$
53–106	0.41	1.11	0.72		33.2	Fe^{3+} octahedral, glass
	1.15	2.25	0.80		44.6	Fe^{2+} octahedral, glass
					22.2	Fe^{2+} and Fe^{3+}, $(Co, Fe)_3O_4$
106–180	0.43	1.21	0.85		33.3	Fe^{3+} octahedral, glass
	1.17	2.39	0.65		28.4	Fe^{2+} octahedral, glass
					38.3	Fe^{2+} and Fe^{3+}, $(Co, Fe)_3O_4$
40.0 mol % CoO, 40.0% Fe_2O_3, 20.0% P_2O_5 (CFP25)						
< 53	0.45	1.08	0.77	–	32.4	Fe^{3+} octahedral, glass
	1.15	2.34	0.79	–	33.3	Fe^{2+} octahedral, glass
				–	34.3	Fe^{2+} and Fe^{3+}, $(Co, Fe)_3O_4$
53–106	0.38	1.17	0.72	–	22.8	Fe^{3+} octahedral, glass
	1.14	2.31	0.75	–	27.2	Fe^{2+} octahedral, glass
	0.36	0.07	0.68	493	40.4	Fe^{3+}, tetrahedral and octahedral, $(Co, Fe)_3O_4$
	0.64	0.30	0.94	448	9.5	$Fe^{2.5+}$, octahedral, $(Co, Fe)_3O_4$

* $\pm 0.5\,mm\,sec^{-1}$ in sextets.

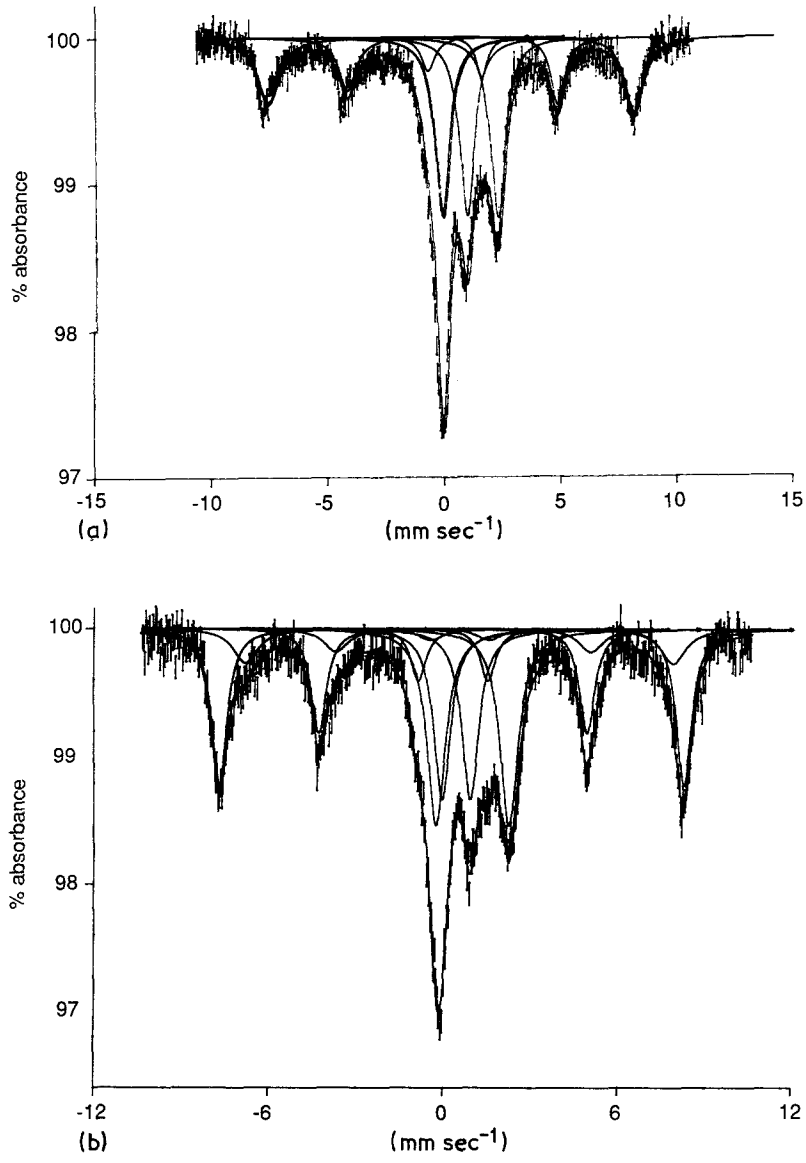

Figure 7 Room temperature Mössbauer spectra of atomized CFP20 of different particle sizes. (a) < 53 μm, (b) 53–106 μm.

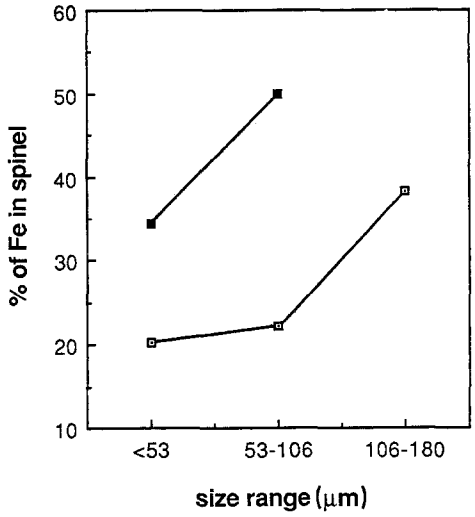

Figure 8 Percent of iron in ferrite phase in rapidly solidified 40% CoO–40% Fe_2O_3–20% P_2O_5 (■ CFP20) and 37.5% CoO–37.5% Fe_2O_3–25% P_2O_5 (□ CFP25).

example, the composition of the spinel in CFP20, 53–106 μm, was 22.7 cation% Co ($Co_{0.68}Fe_{2.32}O_4$, assuming (Co + Fe)/O = 3/4), determined [2] by energy-dispersive analysis of X-rays (EDAX) in the SEM. 50% of the iron in the atomized material is in the ferrite (Table I). That is, 33 wt % of atomized CFP20 with size 53–106 μm is spinel, compared to 77 wt % of "$CoFe_2O_4$" in the overall composition. Even in a melt cooled at $> 10^{4\circ}$ C sec^{-1} (Fig. 5), over 40% of the transition metal oxides in the starting material crystallized as ferrite. This contrasts with the observation of Herczog [16] that phosphate glasses do not readily crystallize ferrites.

3.3.2. Mössbauer parameters

The isomer shifts (δ) in the glass (Table I) indicate that both Fe^{2+} ($\delta > \sim 0.8$ mm sec^{-1}) and Fe^{3+} ($\delta < \sim 0.6$ mm sec^{-1}) are in predominantly six-fold coordination [17]. As is common for glasses, the quadrupole splittings and linewidths are too large for reliable structural inferences. The glassy phase contained roughly equal amounts of Fe^{2+} and Fe^{3+}, independent of both composition and particle size (Table I). This shows, first of all, that appreciable reduction occurred during the short (< 5 min) melting time. Furthermore, the rate of reoxidation of the Fe^{2+} was slow enough compared to the cooling rate that the Fe^{2+}/Fe^{3+} ratios were frozen at essentially the same value, regardless of particle size and composition.

The spectrum containing the largest ferrite peaks (CFP20, 53–106 μm Fig. 7b) exhibited clear asymmetry in the Zeeman pattern, allowing it to be fit to two sextets whose Mössbauer parameters are listed in Table I. These values agree well with previous Mössbauer work [18–20] on $Co_xFe_{3-x}O_4$ with $0 < x < 1$. The larger sextet results from overlapping Fe^{3+} tetrahedral and octahedral patterns, hence its large linewidth compared to most crystals. The broad shoulders that make up the second sextet give an isomer shift and magnetic hyperfine field typical of octahedral "$Fe^{2.5+}$" that is Fe^{2+} and Fe^{3+} that exchange a valence electron in a time shorter than the lifetime of the Mössbauer transition, 10^{-7} sec. This latter sextet may itself be an envelope of several sites, each with a different number of cobalt nearest neighbours [21]. This might explain the very broad linewidth compared to most iron sites in crystals. The listed quadrupole splitting for this sextet envelope may have little absolute significance for this reason; the quadrupole splittings in most magnetic spinels are essentially zero.

3.4. Microstructural studies

Fig. 9 shows SEM micrographs of atomized CFP25 that has been sieved to < 45 μm. The particles in this and the other small size ranges were predominantly spherical, and no satellite formation was observed (that is, small particles were not stuck to larger particles). This indicates that the desired conditions of solidification without collision with nearby particles or other surfaces were achieved.

The bottom photograph shows a single particle from this sample, taken in backscattered mode. The enhanced contrast between the faint light crosses,

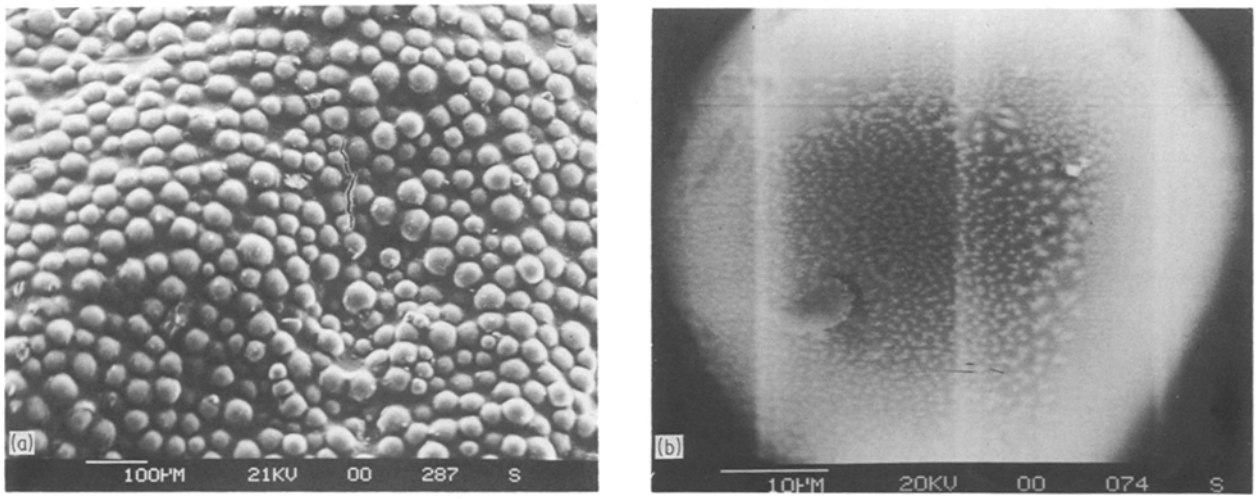

Figure 9 Scanning electron micrograph of atomized 37.5% CoO–37.5% Fe_2O_3–25% P_2O_5 (CFP25 sieved to < 45 μm. (a) representative powder. (b) single particle photographed in backscattered mode to enhance the contrast between the ferrite crystals (light cross-shaped features) and the phosphate glass matrix.

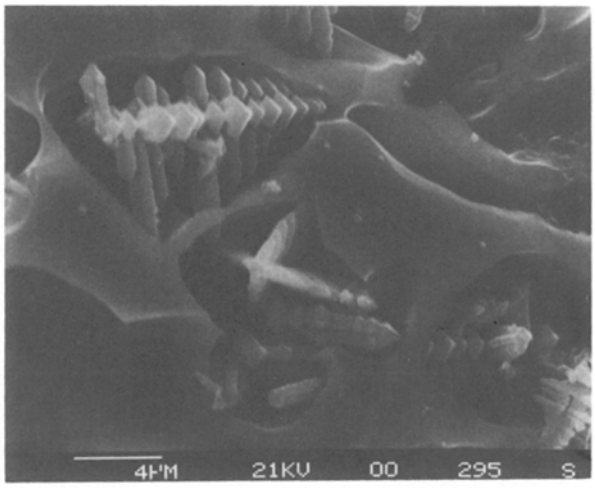

Figure 10 Scanning electron micrograph of atomized 37.5% CoO–37.5% Fe_2O_3–25% P_2O_5 (CFP25) after etching in dilute HCl, showing (Co, Fe)$_3O_4$ crystals in a cobalt–iron–phosphate glass matrix.

$\sim 2\,\mu$m in width, and the matrix shows that the matrix has a lower average atomic number, and hence a higher phosphorus content than the crosses. The shape and composition (that is, less P) of these crosses suggest spinel crystals.

Fig. 10 shows CFP25 $< 45\,\mu$m that has been etched in HCl solution for 15 min. Well developed spinel dendrites $< 10\,\mu$m across and 15–25 μm long have grown parallel to $\langle 1\,0\,0 \rangle$ directions, indicated by their four-fold symmetry. Transition metals, especially iron, greatly increase the corrosion resistance of phosphate glasses [22]. The preferential etching of the phosphate matrix immediately around the dendrites indicates that the melt was depleted of iron (and presumably cobalt) at the crystal interface, suggesting that the crystallization was diffusion controlled.

The growth habit of these spinel precipitates (Fig. 10) reinforces the interpretation that the surface features in Fig. 9 are spinel crystals. It is not clear from either of these micrographs whether growth began on the droplet surfaces or in the bulk. The crystals in Fig. 9 are much smaller than those in Fig. 10. The surface is the most rapidly cooled part of the droplets, and crystals nucleated there would be able to grow much larger as they grew into the more slowly cooled interior of the droplet. It should also be pointed out that the atomized material was accompanied by appreciable amounts of fine Al_2O_3 fibres, eroded from the crucible insulation during atomization. These could have formed heterogeneous nucleation sites on the droplets, thwarting the capability of atomization to provide high undercoolings.

It is evident from Fig. 10 that some of the ferrite crystals were lost during etching, either dissolving or dropping out of the glassy matrix and getting rinsed away.

4. Conclusions

Rapidly solidified cobalt ferrite has been produced in a phosphate glass matrix using gas atomization of $CoFe_2O_4$–P_2O_5 melts. The glass contained approximately equal proportions of Fe^{2+} and Fe^{3+}, regardless of composition and particle size. On the other hand, the ratio of iron in the spinel to iron in the glass increased with increasing particle size and with decreasing P_2O_5 content in the starting composition. These results suggest that the redox kinetics were much slower than crystallization kinetics, perhaps because the surface solidified around the molten interior, preventing re-oxidation of the Fe^{2+} but allowing internal crystallization. The highest fraction of spinel observed in this work, in powders which contained only spinel and glass, was 33 wt %.

Calculations show that for oxide melts, droplet size strongly determines the cooling rate achieved by atomization, with an increase in droplet size of three orders of magnitude resulting in a decrease in cooling rate of approximately five orders of magnitude. The calculations indicate that oxide melts at 1500° C experience cooling rates of $< 10^{6}$° C sec^{-1} for 10 μm droplets and $< 4 \times 10^{4}$° C sec^{-1} for 100 μm droplets.

Acknowledgements

This work was supported by the US Department of Energy, Grant No DE-FG02-84ER451. The authors express their appreciation to Brian Leibowitz for assistance in the design of the atomization chamber; Dr Norio Nogita of Toyo Kohan Ltd. for suggesting the atomizing nozzle design; Dr Enrique Lavernia for discussions of heat transfer coefficient calculations; and Dr Dunbar Birnie for the use of his cooling rate calculation programs. The Mössbauer portion of this work was supported by NASA Grant NSG-7604 to Professor Roger G. Burns of the Department of Earth, Atmospheric, and Planetary Sciences at MIT whose assistance and counsel are gratefully acknowledged.

References

1. A. REVCOLEVSCHI and J. LIVAGE, in "Ultrarapid Quenching of Liquid Alloys", edited by H. Herman (Academic Press, New York, 1981) p. 73.
2. M. R. DE GUIRE, G. KALONJI and R. C. O'HANDLEY, *J. Amer. Ceram. Soc.* submitted.
3. N. J. GRANT, *J. Met.* **35** (1983) 20.
4. S. J. SAVAGE and F. H. FROES, *J. Met.* **36** (1984) 20.
5. H. LUBANSKA, *J. Met.* **22** (1970) 45.
6. G. RAI, E. LAVERNIA and N. J. GRANT, *J. Met.* **37** (1985) 22.
7. E. Y. TING, ScD Thesis. Cambridge, Massachusetts (1984).
8. E. J. LAVERNIA, unpublished work.
9. D. P. BIRNIE III and M. D. DYAR, *J. Geophys. Res.* **91** (1986) 509.
10. "CRC Handbook of Chemistry and Physics", 60th edn. edited by R. C. Weast (CRC Press, Boca Raton, Florida, 1980).
11. J. SZEKELY and N. J. THEMELIS, in "Rate Phenomena in Process Metallurgy" (Wiley Interscience, New York, 1971) p. 237.
12. F. P. INCROPERA and D. P. DEWITT, in "Fundamentals of Heat Transfer" (John Wiley, New York, 1981) Appendix A4.
13. M. R. DE GUIRE, T. R. S. PRASANNA, G. KALONJI and R. C. O'HANDLEY, *J. Amer. Ceram. Soc.* **70** (1987) 831.
14. M. D. DYAR, *Am. Mineral.* **69** (1984) 1127.
15. M. SUGIMOTO, T. TAKAHASHI, H. KAKINUMA, N. HIRATSUKA and K. NAYA, in "Proceedings of the Fourth International Conference on Ferrites", Part II, San Francisco, 1984, edited by F. F. Y. Wang (American Ceramic Society, Columbus, Ohio, 1985) p. 609.

16. A. HERCZOG, *Glass Ind.* **47** (1967) 445.
17. M. R. DE GUIRE, R. C. O'HANDLEY, G. KALONJI and M. D. DYAR, *J. Non-Cryst. Solids* **81** (1986) 351.
18. E. DE GRAVE, R. LEYMAN and R. VANLEERBERGHE, *Phys. Lett.* **97A** (1983) 354.
19. M. K. FAYEK and A. A. BAHGAT, *Z. Phys. B* **46** (1982) 199.
20. P. J. MURRAY and J. W. LINNETT, *J. Phys. Chem. Solids* **37** (1976) 619.
21. H. FRANKE and M. ROSENBERG, *J. Magn. Magn. Mater.* **4** (1977) 186.
22. B. C. SALES, M. M. ABRAHAM, J. B. SALES and L. A. BOATNER, *J. Non-Cryst. Solids* **71** (1985) 103.

Received 25 January
and accepted 10 June 1988